Simulation of debris flow on an instrumented test slope using an updated Lagrangian continuum particle method

Fávero Neto, Alomir H.; Askarinejad, Amin; Springman, Sarah M.; Borja, Ronaldo I.

DOI
10.1007/s11440-020-00957-1

Publication date
2020

Document Version
Accepted author manuscript

Published in
Acta Geotechnica

Citation (APA)
Fávero Neto, A. H., Askarinejad, A., Springman, S. M., & Borja, R. I. (2020). Simulation of debris flow on an instrumented test slope using an updated Lagrangian continuum particle method. *Acta Geotechnica*, *15*(10), 2757-2777. https://doi.org/10.1007/s11440-020-00957-1

Simulation of debris flow on an instrumented test slope using an updated Lagrangian continuum particle method

Alomir H. Fávero Neto[1] · Amin Askarinejad[2] · Sarah M. Springman[3] · Ronaldo I. Borja[1,*]

[1]Department of Civil and Environmental Engineering, Stanford University, Stanford, CA 94305, USA. *E-mail: borja@stanford.edu
[2]Department of Geoscience and Engineering, Delft University of Technology, The Netherlands
[3]Department of Civil, Environmental and Geomatic Engineering, ETH Zürich, Switzerland

Summary. We present an updated Lagrangian continuum particle method based on smoothed particle hydrodynamics (SPH) for simulating debris flow on an instrumented test slope. The site is a deforested area near the village of Ruedlingen, a community in the canton of Schaffhausen in Switzerland. Artificial rainfall experiments were conducted on the slope that led to failure of the sediment in the form of a debris flow. We develop a 3D mechanistic model for this test slope and conduct numerical simulations of the flow kinematics using an SPH formulation that captures large deformation, material non-linearity, and the complex post-failure movement of the sediment. Two main simulations explore the impact of changes in the mechanical properties of the sediment on the ensuing kinematics of the flow. The first simulation models the sediment as a granular homogeneous material, while the second simulation models the sediment as a heterogeneous material with spatially varying cohesion. The variable cohesion is meant to represent the effects of root reinforcement from vegetation. By comparing the numerical solutions with the observed failure surfaces and final free-surface geometries of the debris deposit, as well as with the observed flow velocity, duration of flow, and hotspots of strain concentration, we provide insights into the accuracy and robustness of the SPH framework for modeling debris flow.

1 Introduction

The past decades have seen significant development in computational methods for problems in fracture mechanics, damage modeling, strain localization, and unsaturated soil mechanics. For this type of problems, the finite element method remains the preferred computational platform [35, 43, 52, 53, 62, 73, 75], even as a number of continuum particle methods have also emerged as

viable alternatives in recent years [35, 58–60, 62]. However, when it comes to debris flow modeling, where the motion is so chaotic that element connectivity is difficult to impose, the finite element method may not be an appropriate platform to use, since it suffers from severe mesh distortion that impacts on its accuracy and overall performance. For this type of problem, continuum particle methods may have some distinct advantages in that they do not rely on element connectivity, and thus, they serve as more natural alternatives to the finite element method.

This paper addresses the modeling of landslides and debris flows, which are geologic hazards that occur in many parts of the world. Each year, numerous lives and millions of dollars in property damage have been lost as a result of these phenomena. Despite considerable advances in modeling the initiation of landslides [10–12, 44], predicting the ensuing debris flows and their aftermath remains elusive. Over the years, theoretical models and computational simulation tools have been developed for modeling debris flows [30, 44, 66]. As noted earlier, continuum-based particle methods such as the material point method [5, 27, 64], reproducing kernel particle method [23, 56], peridynamics [34], and the smoothed particle hydrodynamics [16–19, 22, 28, 29, 32, 37, 38, 45–49, 74] are preferable techniques because they can accommodate very large deformations and do not suffer from severe mesh distortion. Discrete element methods (DEM) share the same desirable features [20, 24, 31, 33, 54, 67, 68, 72]; however, they lack scalability to problems larger than laboratory sizes.

Regardless of the computational platform, a theoretical formulation based on an objective stress rate must be employed in the finite deformation range. Currently, a majority of the computational frameworks for finite deformation analysis still employ the classical hypoelastic formulation in which either the Jaumann stress rate or (less frequently) the Green-Naghdi stress rate is used [8]. Such formulations need to address the lingering concern that there may not be a unique stress rate, and so, two or more solutions could be obtained for the same boundary-value problem. Furthermore, the stress-point integration algorithms available for this class of stress rates are not compatible with the implicit return mapping algorithm that is now widely used in computational plasticity [8, 55].

An alternative to the classical hypoelastic formulation is a hyperelastic formulation, which completely bypasses the need to define an objective stress rate. The latter framework can be combined with plasticity theory, as demonstrated in References [7, 9, 13, 15, 61], and recently in the context of the smoothed particle hydrodynamics (SPH) technique by Fávero Neto and Borja [26], who employed hyper-elastoplasticity with a multiplicative split of the deformation gradient [39, 41, 71], to model granular flow. In the latter formulation, the kinematical relationships are expressed either in updated or total Lagrangian form, which makes it suitable for solid deformation characterization that requires a material description.

We should note that Lagrangian SPH kernels had been proposed and studied in the past [6, 50, 69, 70]; however, this was the first time they were applied within the context of the SPH method to simulate granular flows. In the SPH method, continuum material properties and state variables are stored in the memory of the particles, and are continuously updated at each time step to reflect not only their own state of deformation but also the changing configurations of their nearest-neighbor particles. Fávero Neto and Borja [26] validated their model against laboratory test data on dry granular flows, including data from column collapse tests and inclined flume tests on dry sand.

This paper takes one step further and showcases the robustness of the aforementioned SPH technique for capturing the kinematics of water-saturated debris flow resulting from the failure of an instrumented test slope in Ruedlingen, Switzerland. The analyses presented in this paper are unique in that the test slope was full-scale in size and not laboratory-size, and that the sediment that failed was nearly saturated and not dry. A total stress analysis is employed assuming the sediment to be a cohesive-frictional material deforming at a constant volume. As for the cohesion of the material, it was taken as the likely effect of partial saturation and root reinforcement from trees and other forms of vegetation at the test site. The Ruedlingen test slope is one of very few extensively instrumented test slopes that failed as a debris flow, and provides an invaluable dataset against which any debris flow model may be validated. Quantitative validation of an SPH model *at the field scale*, which is very rare in the literature, is the main contribution of this work.

2 Governing equations

We briefly summarize the governing equations for the problem at hand. For a more detailed account of the large deformation SPH framework in Lagrangian form, the reader is referred to Fávero Neto and Borja [26] and references therein.

Let $\mathcal{B}$ denote the problem domain bounded by the surface $\partial\mathcal{B} = \overline{\partial\mathcal{B}_v \cup \partial\mathcal{B}_t}$, where the overline denotes a closure, with $\partial\mathcal{B}_v \cap \partial\mathcal{B}_t = \varnothing$. The strong form of the boundary-value problem is given by

$$\frac{1}{\rho_0}\mathrm{DIV}(\boldsymbol{P}) + \boldsymbol{g} = \boldsymbol{a} \quad \text{in } \mathcal{B} \times t \tag{1}$$

$$\boldsymbol{v} = \bar{\boldsymbol{v}} \quad \text{on } \partial\mathcal{B}_v \times t \tag{2}$$

$$\boldsymbol{P} \cdot \boldsymbol{N} = \boldsymbol{t}_0 \quad \text{on } \partial\mathcal{B}_t \times t \tag{3}$$

subject to initial conditions $\boldsymbol{u} = \boldsymbol{u}_0$, $\boldsymbol{v} = \boldsymbol{v}_0$, and $\boldsymbol{a} = \boldsymbol{a}_0$ at $t = 0$. Here, $\boldsymbol{P}$ is the first Piola-Kirchhoff stress tensor, $\boldsymbol{N}$ is the outward unit normal vector to $\partial\mathcal{B}_t$ in the reference configuration, DIV is the Lagrangian divergence operator, ρ_0 is the pull-back mass density in the reference configuration, $\boldsymbol{g}$ is the gravity

acceleration vector, $\boldsymbol{u}$, $\boldsymbol{v}$, and $\boldsymbol{a}$ are the particle displacement, velocity, and acceleration, respectively, and t is time.

Fávero Neto and Borja [26] presented an SPH discrete operator to calculate the relative deformation gradient tensor for particle i, denoted herein by the symbol $\langle \boldsymbol{f} \rangle_i$. The expression takes the form

$$\langle \boldsymbol{f} \rangle_{i,n+1} = \sum_{j=1}^{N} \frac{m_j}{\rho_{j,n}} \left(\Delta \boldsymbol{u}_{j,n+1} - \Delta \boldsymbol{u}_{i,n+1} \right) \otimes \boldsymbol{\nabla}_n W_{ij} + \mathbf{1}, \tag{4}$$

where W is the kernel function, m_j and ρ_j are the total mass and mass density of particle j, respectively, $\Delta \boldsymbol{u}_i$ is the incremental displacement of particle i, and $\boldsymbol{\nabla}_n$ is the gradient operator taken with respect to the configuration at time t_n. For a given constitutive relationship, the relative deformation gradient is used to update the symmetric Kirchhoff stress tensor $\boldsymbol{\tau}$ using a multiplicative plasticity algorithm that preserves the return mapping scheme of the infinitesimal theory [55]. From the calculated stresses, the acceleration at time t_{n+1} may be obtained using Newton's second law. Employing SPH averaging, we get

$$\boldsymbol{a}_{i,n+1} \equiv \left\langle \frac{d\boldsymbol{v}}{dt} \right\rangle_{i,n+1} = \sum_{j=1}^{N} m_j \frac{(\boldsymbol{P}_{i,n+1} + \boldsymbol{P}_{j,n+1})}{\rho_{i,n} \rho_{j,n}} \cdot \boldsymbol{\nabla}_n W + \boldsymbol{g}_i \,. \tag{5}$$

Furthermore, the mass density can be updated through the kinematic relationship

$$\rho_{i,n+1} = \frac{\rho_{i,n}}{\overline{J}_{i,n+1}}, \tag{6}$$

in which $\overline{J}$ is the Jacobian of the relative deformation gradient.

The constitutive relationship is provided by a hyperelastic-perfectly plastic non-associative Drucker-Prager model. The elastic stored energy function is given by the Henky model

$$\Psi = \frac{1}{2} K \ln(J_e)^2 + \mu \|\boldsymbol{e}^{\mathrm{e}}\|^2 \,, \tag{7}$$

where K and μ are the elastic bulk and shear moduli, respectively, J_e is the Jacobian of the elastic deformation gradient tensor, and $\boldsymbol{e}^{\mathrm{e}}$ is the deviatoric part of the logarithmic elastic principal stretches. The yield criterion is given by

$$\mathcal{F} = \sqrt{3/2} \|\boldsymbol{s}\| + \alpha_\phi p - \kappa \leq 0 \,, \tag{8}$$

where $\boldsymbol{s}$ is the deviatoric part of the symmetric Kirchhoff stress tensor $\boldsymbol{\tau}$, $p = \mathrm{tr}(\boldsymbol{\tau})/3$, and α_ϕ and κ are Drucker-Prager material parameters related to the internal friction angle ϕ and cohesion c of the Mohr-Coulomb model, respectively. The relevant expressions relating these parameters are given in [8]. For non-associative flow rule with a deviatoric plastic flow, the plastic potential $\mathcal{Q}$ may be written as

$$\mathcal{Q} = \sqrt{3/2}\|\boldsymbol{s}\| + \alpha_\psi p\,, \tag{9}$$

where α_ψ is the Drucker-Prager parameter associated with the soil's dilation angle ψ. The relevant expressions for the Drucker-Prager parameters α_ϕ, α_ψ, and κ are given in [8].

We note that the Mohr-Coulomb parameters ϕ and c are interpreted herein as *total stress parameters*. In principle, ϕ must be zero under fully undrained condition and complete saturation; however, a non-zero value of the friction angle could develop if the sediment is not fully saturated [14], such as in Ruedlingen where suction stresses were noted. Furthermore, partial drainage could occur in the sediment as it slows down and comes to a stop, thus further mobilizing the friction angle. Finally, as discussed previously and elaborated further in subsequent sections, the value of cohesion may be attributed to the presence of suction stresses and root reinforcements particularly from deforested trees. For the Ruedlingen site, the root reinforcements from those trees are a great source of heterogeneity that could give rise to a spatially varying sediment cohesion.

3 The Ruedlingen test slope

The Ruedlingen test slope is located in northern Switzerland on the bank of the Rhine River, with an elevation of 350 m above sea level. In March 2009, artificial rainfall experiments culminated in failure of the slope in the form of a debris flow. Prior to this failure, extensive instrumentation was installed at the site to measure hydrological and geomechanical properties of the slope sediment during both natural and artificial rainfall. Instruments installed at the site included tensiometers, time domain reflectometers [36], piezometers, slope deformation sensors [2], and earth pressure cells, among others. Before the instrumentation was placed and the experiments could begin, a slope area of approximately 350 m^2 was deforested, and roots were severed around the perimeter at the test site prior to the rainfall experiments that caused the debris flow of March, 2009 [4]. High resolution photogrammetric cameras were also placed at strategic positions to capture and monitor the movement of the sediment. Needless to say, this slope provides invaluable datasets for the study and analysis of a natural slope that failed as a debris flow. In what follows, we provide detailed characterizations of the slope that are relevant for modeling the failure processes.

3.1 Geological characterization

The geological formation in the Ruedlingen area consists predominantly of sedimentary rock, or molasse, which could be confirmed by visual inspection in boreholes and outcrops near the test site [3]. The molasse was composed of

alternating layers of fine-grained sandstone and marlstone, which indicate alternating geomorphological processes of deposition. These processes, in turn, resulted in differential mechanical properties for each layer. Atop the bedrock, the soil horizon is composed mainly of silty sand mixtures with stone eroded from earlier superficial landslides as well as originating from natural weathering of the underlying sedimentary rock.

The sediment-bedrock interface was determined through a series of tests employing the dynamic probing light (DPL) method. These tests were conducted every 2 m, and the criterion for determining whether the bedrock was reached was set to 30 blows per 10 cm of penetration [3]. It was found that the depths of the bedrock top ranged from 0.5 m to over 5 m, and that the right-hand side (RHS) section of the bedrock top was shallower on average than the left-hand side (LHS) section. However, inspection of the sediment after the debris flow of March 2009 showed that intact pieces of the bedrock were present in the sediment at shallower depths, which could have hindered an accurate measurement of the bedrock depth [3, 4]. Figure 1 shows a schematic representation of the sediment profiles where the DPL tests were conducted. The LHS section includes points labeled P1, P2, and M1, while the RHS includes the points P3, P4, and M2 shown in Figure 1.

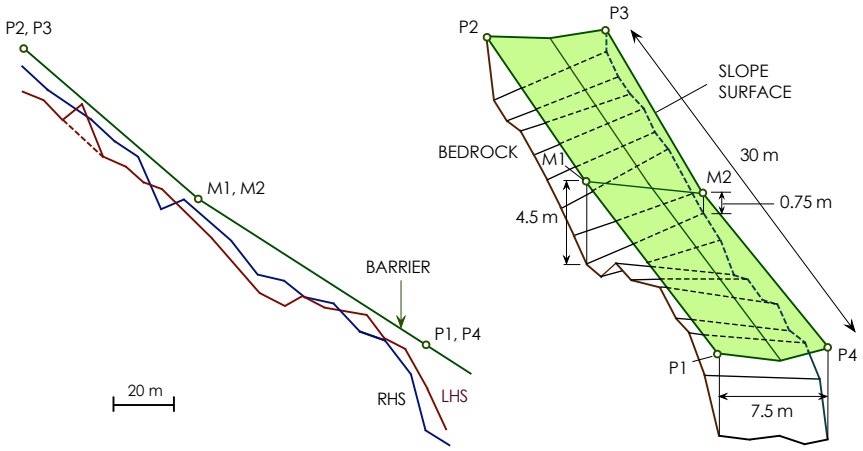

Fig. 1: DPL test results and location. Data after Askarinejad [3].

3.2 Sediment characterization

Based on correlations between results of the DPL tests and the standard penetration tests, Askarinejad [3] concluded that the sediment at the site was

very loose near the surface and medium-dense near the bedrock. Six test pits were excavated around the slope area where disturbed and undisturbed sediment samples were collected and tested in the laboratory to determine their geomechanical properties. Among the tests performed were grain size distribution, Atterberg limits, shear strength, and compaction tests. The results of grain size distribution tests showed that 60% of the sediment is composed of medium to fine sand, 35% silt, and less than 5% is of clay fraction. This composition rendered an average liquid limit of 27%, and a plastic limit of 20%. According to the USCS classification, the sediment at Ruedlingen can be classified as a low plasticity silty sand (SM-ML).

Constant shear undrained (CSU) and drained (CSD) triaxial tests [63] were conducted on undisturbed and disturbed samples in loose and compacted states. Skewed-barrel failure patterns were generally observed, with shear bands forming at approximately 62° with respect to the horizontal. Internal critical friction angles of $\phi_c = 34°$ for the CSU tests, and $\phi_c = 32.5°$ for the CSD tests were determined [3]. Values of internal friction angle as high as $\phi_c = 35°$ were also observed [21].

Standard and modified Proctor tests yielded maximum dry unit weights of 16.35 kN/m^3 and 18.50 kN/m^3, respectively. Similar tests on reconstituted sediment samples yielded minimum and maximum dry unit weights of 12.50 kN/m^3 and 15.30 kN/m^3, respectively. Natural samples from Ruedlingen were measured to have a mean void ratio of 1.0, a natural unit weight of 16.33 kN/m^3, and dry unit weights varying from 11.85 kN/m^3 to 13.77 kN/m^3.

3.3 Influence of vegetation

Three types of vegetation have been identified to be present in the test slope area: trees, shrubs, and herbs [3]. This vegetation formed a network of roots that helped stabilize the slope, by virtue of mechanical reinforcement (i.e., pull-out resistance), and through increased matric suction in the sediment [65]. Lateral root cohesion and root reinforcement were investigated by Schwarz [51], by measuring the pull-out force as a function of root diameter. He found out that roots larger than 1–2 mm in diameter mobilized full friction and would break instead of slip when pulled, generating an estimated frictional stress of 5 kPa. Furthermore, based on his results he created a root reinforcement map of the added shear strength to the sediment in the form of additional cohesion. As can be seen from Figure 2, the added root cohesion varies from 1 kPa to as high as 90 kPa.

Based on the work of Schwarz [51], Askarinejad [3] also considered two different mechanisms of added strength due to the network of roots. The first mechanism, called lateral root cohesion, was considered to be the shear strength added to the slope perimeter and is attributed to the shallower roots up to a depth of 0.3 m below the surface. This added reinforcement is estimated to be equivalent to a cohesion of 4 kPa. The second mechanism, root reinforcement, is based on the map of Figure 2 and could extend to the

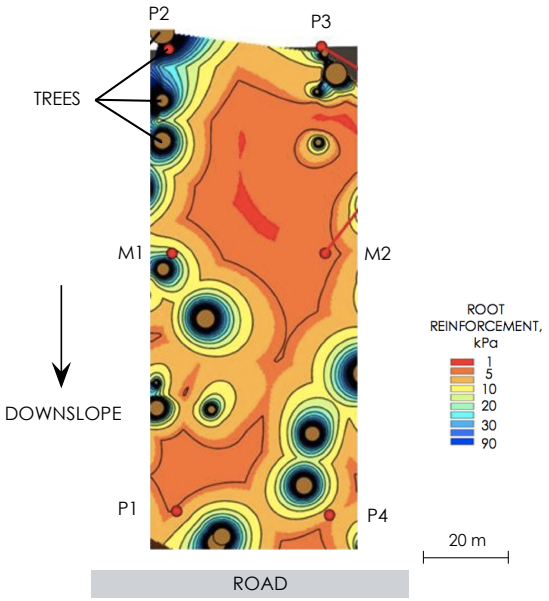

Fig. 2: Root reinforcement as determined by Schwarz [51]. Color bar is added root cohesion in kPa.

bedrock. This added resistance is due to the deeper roots of trees that were cut. The importance of root reinforcement cannot be overstated. In fact, the presence of roots was considered to be one of the main reasons why the slope remained stable for so many years despite the numerous intense rainfalls it has experienced in the past. Failure was triggered after lateral root cohesion was diminished by severing them at the boundaries of the test site, and upon intensification of the rainfall experiments that led to saturation.

3.4 Slope description

The deforested Ruedlingen hillside slope had an average inclination of 38°, with minimum and maximum inclinations of 35° and 42°, respectively. The upper part of the slope was concave, while from its midsection downwards, the slope was slightly convex. Topographic measurements were performed at the locations of every instrument on the slope, as well as at pits and boreholes, trees, and other landmarks in the area. Figure 3 shows the locations of these measurement points, which were used to generate a three-dimensional model of the slope surface as well as the bedrock (from DPL points, boreholes and pits). From the above information, a 3D model of the sediment layer and bedrock top could be generated.

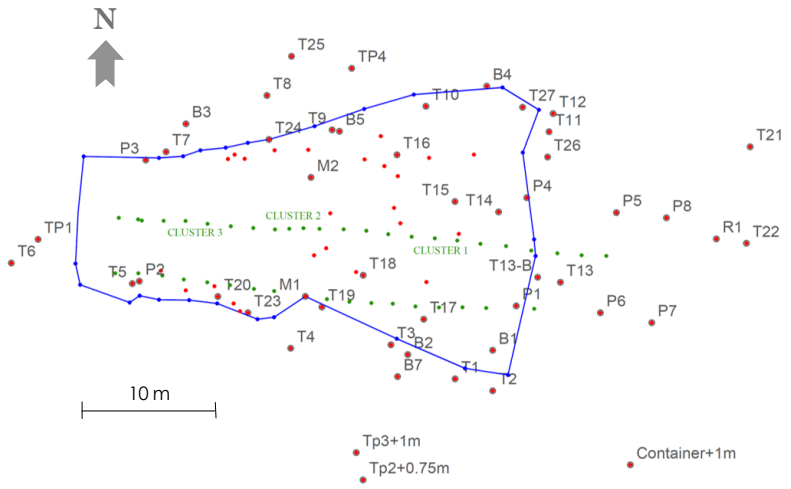

Fig. 3: Topographic measurement points at Ruedlingen test slope. B = boreholes, P = corner points, M = middle points (on the longitudinal borders), T = trees, Tp = test pits.

3.5 Slope failure description

In the early hours of 17 March 2009, approximately 130 m^3 of sediment failed and moved down the slope, leaving a failure surface approximately 17 m long and 7 m wide across the hillside, with a total area of 120 m^2 (or a horizontal projection of 97 m^2), and average depth of 1.09 m (1.33 m for the horizontal projection). All the sediment inside the failure scar was carried down by the flow, and the bedrock was visible. The debris flow lasted approximately 11 s, with maximum runout velocities of around 3.0 m/s, calculated from the high resolution images and videos [3]. Figure 4 shows the location of the failure scar inside the horizontal projection of the test site.

Between October 2008 and March 2009, intense precipitations occurred at the site but the slope remained stable. However, following heavy rains in March 2009, the superficial roots were severed around the instrumented site, and the artificial rainfall experiment resumed on 16 March 2009, continuing until the slope failed the next day [3]. Some hours before the slope failed, continuous monitoring of the inclinometers detected the formation of a shear band approximately 80 cm below the surface of the upper right quadrant of the slope [1]. Photogrammetric cameras recorded the formation of a tension crack also on the upper right part of the slope. This crack widened and spread to the LHS of the field, after which, sliding took place and accelerated in a stepwise fashion. The entire mass of sediment went downwards and was channeled

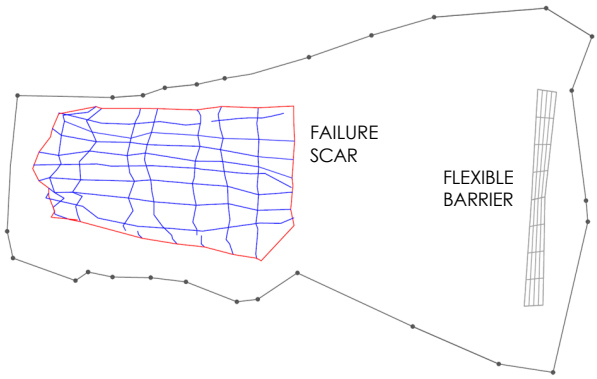

Fig. 4: Failure scar on the upper-right portion of the Ruedlingen slope.

to the RHS by tree stumps, eventually coming to rest in front of the flexible barrier at the bottom of the slope.

Data provided by the slope deformation sensors from the ensuing moments before failure showed that movements on the RHS were faster than on the LHS, which was attributed to shallower sediment and less root reinforcement in that area [3, 57]. Furthermore, data showed that failure developed at around 1.3 m below the surface on the RHS and propagated horizontally to the LHS at a similar depth. Measured values of pore water pressure, before and during the failure, indicated that suction decreased from around 5 kPa to an average of 0.7 kPa in the upper part of the slope, while the lower parts of the slope remained unsaturated up to depths of 50 cm to 90 cm, with negative pore pressure magnitudes as high as 2 kPa. Table 1 summarizes the information presented above.

4 SPH model and simulation setup

We now generate a 3D model of the Ruedlingen test slope using the topographic data and mechanical properties of the sediment described in the previous sections. First, we create a 3D terrain model of the slope that later serves as the basis for the creation of SPH particles. We perform two main simulations to explore the impact of changes in the mechanical properties of the sediment on the ensuing kinematics and movement. In the first simulation, herein referred to as F1, we model the sediment as a cohesionless homogeneous material, where the absence of cohesion is based on the assumption that the sediment was fully saturated and that no root reinforcement existed within the sediment. In the second simulation, called F2, we consider the sediment as a heterogeneous material with spatially varying cohesion, where the variable cohesion is meant to represent the effects of root reinforcement and capillary

Table 1: Summary of data related to Ruedlingen test slope.

Property	**Value**
Failure date	17 March 2009
Altitude	350 m
Test area	262.5 m^2
Slope inclination range (average)	35° to 42° (38°)
Bedrock geology	sandstone/marlstone
Soil classification	silty sand (SM)
Sediment depth range	0.5 m to over 5.0 m
Liquid limit of the fines	27%
Plastic limit of the fines	20%
Critical state friction angle range	32° to 34°
Dilatancy angle	0°
Bulk modulus	17,000 kPa
Shear modulus	7,900 kPa
Average unit weight	15.2 kN/m^3
Root cohesion reinforcement range	1 kPa to 90 kPa (*)
Failure area	119 m^2
Average failure depth	1.09 m
Failure volume	approx 130 m^3
Estimated runout velocity	3.0 m/s
Matric suction at failure	$\leq$ 0.7 kPa

(*) Based on lateral root pulling resistance [51].

stresses. The cohesion provided by the presence of roots was found to be significant by Schwarz [51] and Askarinejad [3], and was thought to be the main stabilizing factor during previous stretches of heavy rainfall when the slope remained stable.

We assess the quality of our model and the proposed framework both qualitatively and quantitatively. In terms of qualitative assessment, Askarinejad [1, 3] provides a thorough account of the sequence of events that took place during the failure stage at Ruedlingen, which serves as a basis for comparison with the simulated overall mechanism of failure. In terms of quantitative assessment, the main measurements include the location, area, and volume of displaced sediment; the maximum and average runout velocities; the final depositional configuration in terms of location and shape of the deposit; and the duration of the flow.

Figure 5 shows the CAD model developed for the slope containing the sediment and boundary solid objects [25]. The figure also displays the position of a net used to contain the sediment from an eventual debris flow. This flexible barrier was installed at the site to avoid damage or blockage of a service road located at the toe of the slope (not shown in the 3D representation). Using this CAD model and a pipeline that includes generating a regular grid of points and extracting those intersecting with the solids to determine the SPH

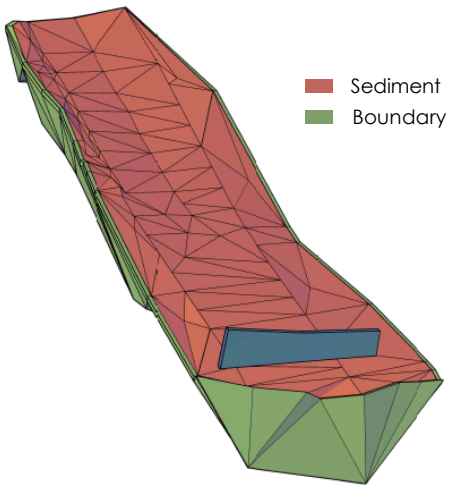

Fig. 5: 3D CAD model of the deforested portion of the Ruedlingen slope.

particles representing the sediment, bedrock, and barrier, we obtain the SPH model shown in Figure 6. The readers are referred to Fávero Neto [25] for further details of this pipeline. The model shown in Figure 6 has a total of 587,508 particles, divided into 387,792 sediment particles, 195,870 bedrock particles, and 3,846 protection net (barrier) particles. The overall dimensions of the model are 34 m $\times$ 17.75 m in planar projection, with a maximum elevation of 30.25 m. These dimensions comprise an area of approximately 500 m^2, and a total volume of 757.0 m^3 of sediment, which is roughly 1.42 times the area, and twice the volume of the deforested test site. The initial distance between particles was set to $\Delta x = 0.125$ m, giving each particle the same mass and initial volume of approximately 1.95×10^{-3} m^3. The initial distance between particles was chosen based on the results of a sensitivity analysis previously conducted by the authors, and corresponds to the more refined particle distribution [26].

Before performing Simulations F1 and F2, we performed a setup simulation to initialize the stresses with the slope under natural, unsaturated conditions. The setup simulation is an essential part of the other two simulations, since the kinematics of failure are dependent on the history of stress and deformation in geomaterials. Some insights into the stability of the slope prior to the ensuing debris flow can also be gained from this simulation. Sediment properties for this simulation are summarized in Table 2.

For the setup simulation, the particles initially at rest were subjected to a body force (gravity) applied downwards in the z-direction. Gravity acceleration was increased gradually from zero to 9.81 m/s^2 over 1000 steps to

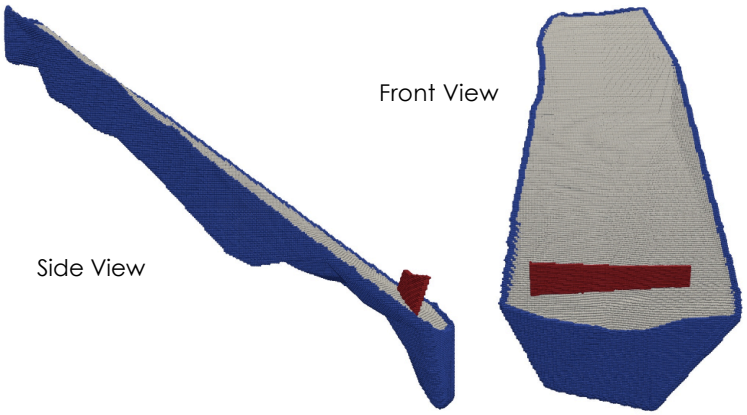

Fig. 6: SPH particle model for the Ruedlingen slope.

Table 2: Sediment properties for the setup simulation.

Property	**Value**
Internal friction angle, ϕ	34°
Cohesion, c	5 kPa
Bulk modulus, K	17,000 kPa
Shear modulus, G	7,846 kPa
Unit weight, γ	15.0 kN/m^3
Monaghan artificial viscosity, α	0.2
Monaghan artificial viscosity, β	0.4
Numerical sound speed, c_{s0}	105 m/s
Initial particle distance, Δx	0.125 m
Smoothing length, h	0.1875 m

avoid numerical instabilities. The total simulation spanned over 2000 steps of $\Delta t = 0.0003$ s each, with final time $t = 0.6$ s. For this and all subsequent simulations, the smoothing length coefficient was set at $k_h = 1.5$, which resulted in a smoothing length $h = 0.1875$ m, providing a good balance between accuracy and computing time. These numbers were based on previous parametric studies conducted by the authors [26]. Since the sediment is not expected to deform significantly during the gravity loading phase, the dilation angle does not play a significant role in the calculations, and is thus set equal to zero. Furthermore, for all the remaining simulations the dilation angle was also set to zero, in agreement with the plastic potential function of Equation (9) and is a common practice when simulating debris flows [18, 26, 28, 45, 49].

The states of stress and elastic deformation, as well as densities and positions of the particles generated from the setup simulation were used as input

for Simulations F1 and F2. For Simulation F1, we kept the same parameters as in the setup simulation, but reduced the cohesion to accommodate partial saturation after the rainfall experiments. Hence, sediment was assumed to be homogeneous with $\phi_c = 34°$ and $c = 0$, and with only the gravity load acting on the slope. The entire simulation lasted approximately $t = 20$ s of solution time.

For Simulation F2, we utilized the same parameters except we increased the cohesion. The spatial variability of cohesion was based on the root reinforcement map of Schwarz [51] shown in Figure 2, and applied throughout the sediment depth. Figure 7 shows the SPH model for this simulation, where colors of the particles indicate their local cohesion. In this figure, the dark-blue area is cohesionless, while the light-blue area corresponds to a constant cohesion of $c = 0.7$ kPa. The white areas coincide with the locations of larger tree roots, and were modeled with $c = 2$ kPa.

It is worth mentioning that the decrease of soil strength (cohesion) to initiate failure in both simulations is a natural consequence of the loss of suction in a soil that was initially partially saturated. This corresponds to a cohesion softening [8], which is a realistic representation of the loss of strength due to increased saturation [61].

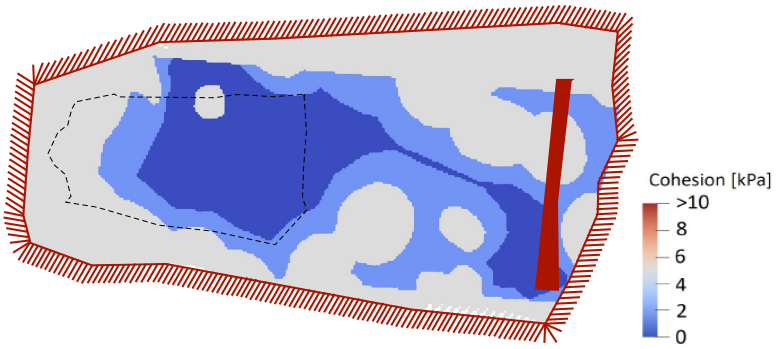

Fig. 7: Particle cohesion for simulation with root reinforcement, based on the work of Schwarz [51] and Figure 2. Dashed line = position of failure scar; red area = flexible barrier.

In all simulations, both bedrock and barrier particles representing the solid boundaries were given the same properties as those of the sediment particles. However, as described by Fávero Neto and Borja [26], boundary properties do not evolve in time. Furthermore, the only boundary properties that have an impact on the sediment particles are density and mass, but they were held constant throughout the simulation. Numerical viscosity was also added to the problem using the standard Monaghan artificial viscosity [42], with parameters

$\alpha = 0.2$ and $\beta = 0.4$. Finally, the variant of dynamic boundary condition presented by Fávero Neto and Borja [26] was used in all the simulations to prevent boundary penetration.

5 Debris flow with homogeneous sediment

In order to better illustrate and compare the results of Simulations F1 and F2, we selected three longitudinal and four transversal cross sections to plot the relevant results, see Figure 8. Two longitudinal cross sections were chosen on the left-hand side (LHS) and right-hand side (RHS) of the failure surface, and joined by a third section on the centerline (CENTER) of the slope. The transversal cross sections correspond to the TOP, MIDDLE, and BOTTOM portions of the failure zone surveyed at the Ruedlingen site, while the fourth section is adjacent to the BARRIER. Figure 8 shows the alignments of all cross sections on the Ruedlingen slope model. Note that they were all selected to be parallel (transversal) or perpendicular (longitudinal) to the barrier. For reference, the observed failure scar is also indicated in this figure.

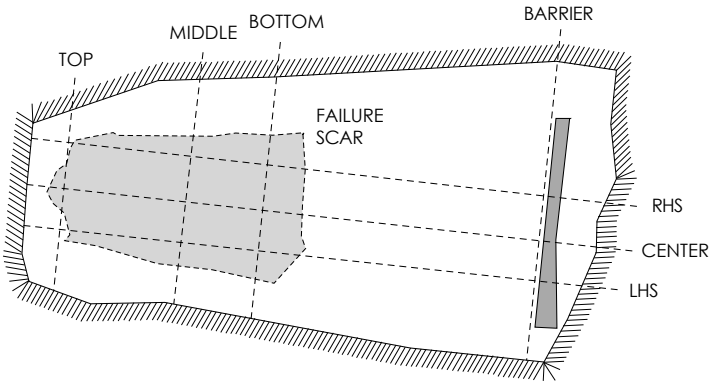

Fig. 8: Longitudinal (LHS, CENTER, RHS) and transversal (TOP, MIDDLE, BOTTOM, BARRIER) cross sections of the Ruedlingen slope.

As noted earlier, the setup simulation involves application of gravity load to the sediment, modeled herein as an unsaturated soil, allowing the particles to reach a state of equilibrium. An equilibrium state furnishes the initial stresses and deformations, as well as provides the equilibrium positions and densities for each particle in the SPH model. Figure 9 presents some of the

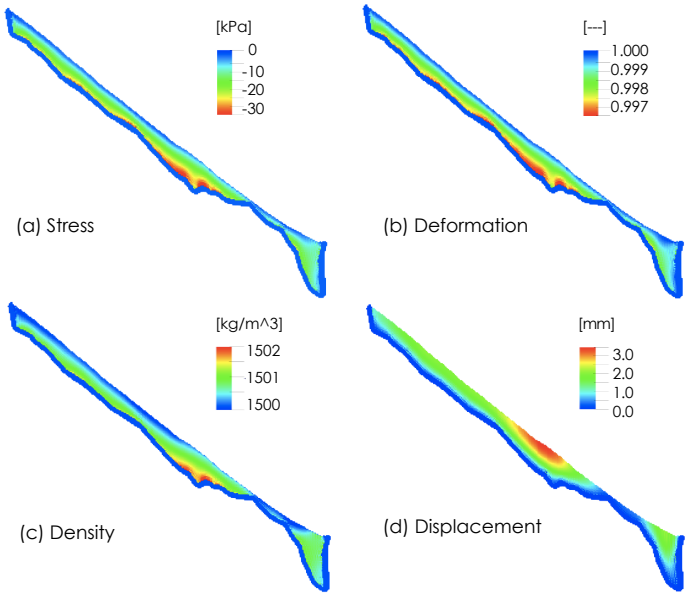

Fig. 9: Final results from setup simulation at the longitudinal centerline of the Ruedlingen slope: (a) Cauchy stress σ_{zz}, (b) elastic left Cauchy-Green deformation b^e_{zz}, (c) total mass density ρ, and (d) total particle displacement $\|\boldsymbol{u}\|$.

results used as input into Simulations F1 and F2, evaluated at a longitudinal section at the center of the Ruedlingen slope.

Results from the setup simulation demonstrate that no significant plastic deformation developed after full application of the gravity load, which implies that the slope was stable in the natural unsaturated condition. In order to trigger instability in the slope for Simulation F1, the apparent cohesion was instantaneously reduced to zero throughout the slope to simulate a reduction in the matric suction due to saturation, while ignoring the effect of root reinforcement. The following subsections present the results of this simulation.

5.1 Quantification of mobilized sediment

We first investigate the scenario in which the cohesion c was reduced to zero throughout the sediment domain. To this end, we ran the entire simulation for about $t = 20$ s of solution time to fully capture the failure processes up until the moment when the transported sediment achieved static equilibrium at the bottom of the slope.

In what follows, we quantify the mobilized area and volume, and analyze the final configuration of the sediment deposit. Figure 10 compares the debris flow zone obtained from the numerical simulation with the one surveyed at the Ruedlingen test site [3]. As shown in this figure, the calculated debris flow zone is more widespread than the one observed in the field – the entire upper portion of the slope mobilized to a certain extent. The failure contour in the simulation comprises an area of approximately 201 m^2, as opposed to 119 m^2 surveyed at the slope site. The discrepancies between the calculated and field results may be attributed to two main causes: (1) the sediment in the field is in fact non-homogeneous with the cohesion varying spatially due to root reinforcement and matric suction, and (2) the mechanical model did not accurately capture the boundary condition at the bedrock-sediment interface.

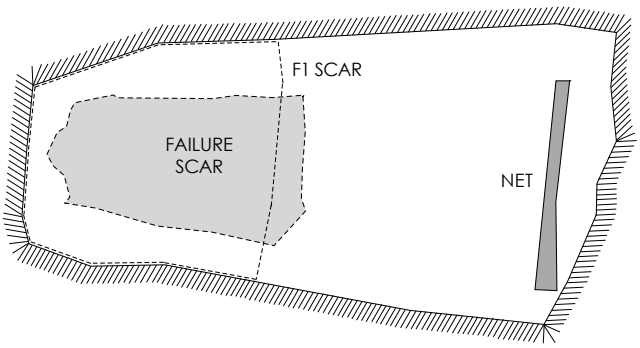

Fig. 10: Comparison of actual failure scar and scar predicted by simulation F1.

As mentioned before, the sediment at the Ruedlingen test slope had considerable lateral root reinforcement especially around the edges, and in the uppermost and lower portions of the slope. Furthermore, the real conditions at the onset of failure were far from being homogeneous, with excess pore-water pressures concentrated in the upper portion of the slope. The fact that parts of the slope were not fully saturated implies the presence of suction stresses, which, along with root reinforcement, would increase the strength of sediment in those areas. This heterogeneity was not taken into account in the simulation.

Regarding the sediment-bedrock interface, it has been reported by Askarinejad [3] that the bedrock surface determined by DPL tests might have been inaccurate as unweathered rock fragments had been discovered inside the mobilized sediment at post-failure. This could have significant implications for the failure patterns observed in the field. Furthermore, in order to create a

perfect enclosure for the sediment particles in the simulation, the bedrock was extended all the way to the surface along the model perimeter, creating tapered layers of sediments with their bases sloping inwards. This is not an ideal situation that could have led to unstable sediment in these areas, especially at the upper portion of the slope where inclinations were greater compared to those at the bottom of the slope. Obviously, the assumption of homogeneous sediment properties and the simplified bedrock topography led to a more widespread mobilization of the failed sediment especially in the upper portion of the slope. Nonetheless, even with these limitations, the kinematics and other quantitative results are in good agreement with the measurements at the site, as elaborated further in what follows.

The volume of sediment mobilized during the debris flow at Ruedlingen was measured to be approximately 130 m^3 (Table 1). In our simulation, the mobilized volume was calculated to be around 190 m^3 based on the initial volumes of the particles under the projection of the failure zone. This gives an error of 46%. Using yet another approach, where we calculated the final displacements of all particles and considered only those that displaced more than one kernel radius, $2h$ as part of the mobilized mass, this volume was estimated to be around 61% higher, or 210 m^3. However, this last approach is less accurate since the particles near the surface of the flow path are usually dragged along and can easily displace a distance several times greater than $2h$. There were also localized shallow runs of particles in the lower part of the slope that ended up being counted as part of the mobilized volume. This is discussed further when we provide more details on the flow kinematics.

Figure 11 shows the sediment configurations at the beginning (light-blue and purple areas) and at the conclusion (pink and purple) of the debris flow for the three longitudinal sections of the slope, as well as the surveyed failure surfaces (dark line) at the site. Figure 12 shows the same information for the transversal cross sections. We see that most of the sediment transported in the SPH calculations originated from the top transversal section of the slope, whereas the geometry of the surveyed failure scar suggested that a significant portion of the transported volume was also derived near the bottom transversal section where the failure surface penetrated deeper into the sediment, albeit over a narrower width.

Right in front of the barrier, the shape of the final sediment deposit can only be assessed qualitatively since the actual barrier was a flexible net, whereas the SPH model assumed the barrier to be a rigid wall. A post-failure survey of the debris collected by the flexible barrier is represented by the dark contour shown in Figure 12d. The predicted configuration shows a sediment deposit extending all the way to the top of the barrier, in addition to sediment deposited on the sides of the barrier. These can be attributed in part to the fact that the barrier was assumed to be rigid, and in part to the larger volume of sediment mobilized in the SPH calculations. For reference, Figure 13 shows photographs of the deposited sediment collected by the flexible barrier.

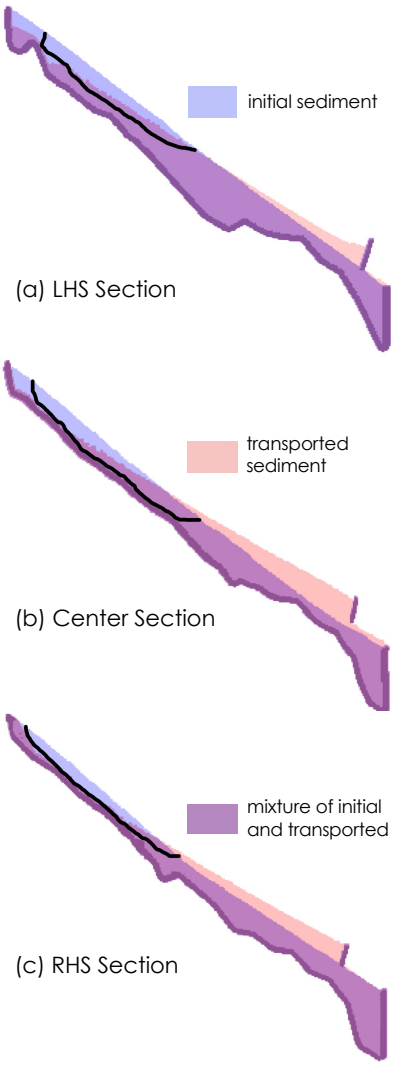

Fig. 11: Final configuration of sediment deposit on three longitudinal sections from Simulation F1. Black outline represents the failure surface surveyed at the Ruedlingen site.

It is worth noting that in the photographs shown in Figure 13, it appears as though all the debris was collected by the net and that there was no accumulation of sediment along the runout path. However, the video footage [1] suggested that the tree stumps and the reinforced sediment downslope projected the debris upward and forward at the failure toe, thus altering the

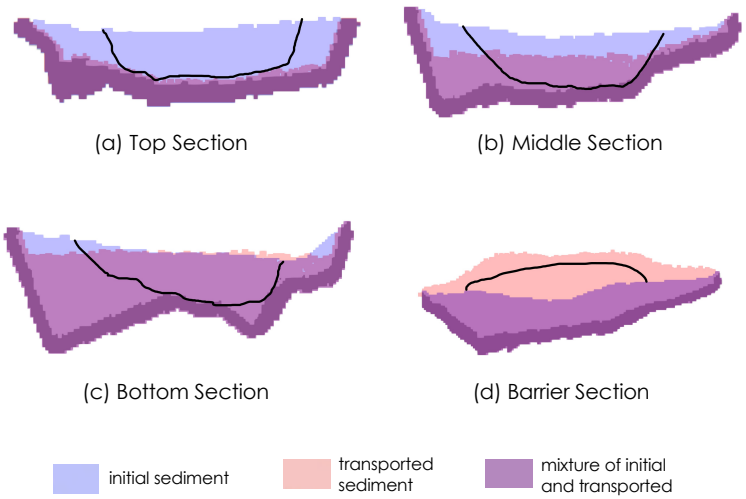

Fig. 12: Final configuration of sediment deposit on four transversal sections from Simulation F1. Black outlines represent the failure surface surveyed at the Ruedlingen site.

Fig. 13: Photographs of the Ruedlingen slope sediment after the debris flow of 17 March 2009. Note the deformation of the debris that accumulated in front of the barrier. Reproduced from [3].

mechanism of deposition that is not reflected in the photographs of Figure 13. Furthermore, prior to taking these aforementioned photographs, some of the sediment not contained by the net was washed out to avoid any debris from bypassing the net and reaching the service road at the bottom of the slope (Askarinejad, private communication).

We should note that whereas the scarp zone may be interpreted to represent a portion of the failure surface, some debris upstream partially filled the failure scar near the bottom of the failure zone. This is evident from Figures 14 and 15, which suggest that the bottom of the failure zone does not necessarily represent the failure surface. To better visualize the failure zone, we make use of the continuum nature of our framework and identify hotspots of deformation, or zones of plastic strain localization. Figures 14 and 15 show these zones at time $t = 0.6$ s, along with the surveyed failure scar at Ruedlingen. For purposes of definition, the strains plotted in these figures are the second invariant of the logarithmic plastic principal strains arising from the multiplicative plasticity formulation. Interestingly, there is better agreement of the surveyed scar at Ruedlingen with the depth and shape of the zones of plastic strain localization than with the calculated free surface at post-failure. It is worth noting that the time $t = 0.6$ s was obtained from simulation F1, and corresponds to the time required to initiate the mobilization of the failure surface.

5.2 Kinematics of triggering and runout

We use two kinematic features to validate our framework, namely, runout velocity and duration of the flow. Askarinejad and co-workers [3, 4] reported that the maximum runout velocity was approximately 3 m/s and that the flow lasted around 11 s. These results were obtained from photogrammetric measurements and a recording of the debris flow published as the supplementary material of Askarinejad et al. (2018) [1]. Figure 16 shows the calculated average, median, and range of runout velocities of the sediment as functions of time. As can be seen from this figure, Simulation F1 resulted in very similar velocities to those reported by Askarinejad [3], with an average velocity close to 1.6 m/s and maximum velocity of approximately 2.9 m/s. Based on these values, the duration of the flow is estimated to be approximately 10.6 s, which is in very close agreement with the previously reported duration of 11 s.

We next assess how well the numerical simulations can identify the hotspots of strain localization and the sequence of failure. Although this is a qualitative comparison, it ensures that the model does capture the most important features of the failure mechanism. For Simulation F1, these features include the sediment depth, bedrock topography, and 3D effects.

As pointed out by Askarinejad and co-workers [3, 4], failure initiated near the upper end of the RHS section of the slope. Inclinometer measurements identified the initiation of strain localization at about 80 cm below the surface in that area. An initial crack was then observed on the surface, which later propagated towards the LHS of the slope. Once this transversal crack had formed spanning a sizable part of the slope width, the sediment started to separate along a tension crack/back scarp and shear. Before the motion started, however, slope deformation sensor measurements had captured the

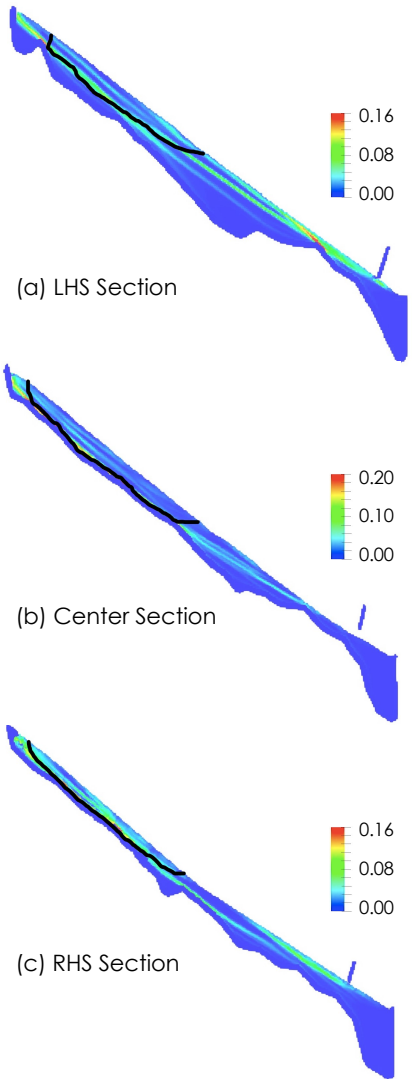

Fig. 14: Accumulated plastic strain at $t = 0.6$ s from Simulation F1. Black outline represents the failure surface surveyed at the Ruedlingen site. Color bar is norm of deviatoric plastic strain.

propagation of an initial failure zone extending all the way to the LHS section, with a nearly constant depth of 1.30 m below the slope surface.

Similar patterns have been observed in our simulation. However, we note that for Simulation F1 there was no localized zone reaching the slope surface on the upper part of the RHS section. Instead, the localized zone extended

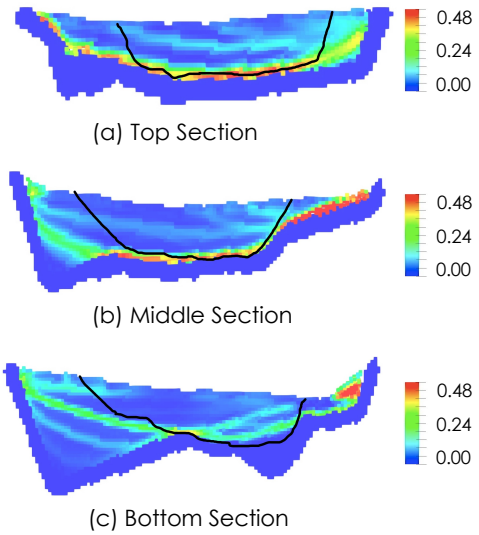

Fig. 15: Accumulated plastic strain at $t = 0.6$ s from Simulation F1. Black outline represents the failure surface surveyed at the Ruedlingen site. Color bar is norm of deviatoric plastic strain.

parallel to the slope at a depth of approximately 1.25 m below the surface, resembling a shear band. It is important to note that this depth corresponds to the sediment-bedrock interface on the RHS section, and this was the main localized zone that mobilized the sediment. The localized zone then propagated to the LHS of the slope at similar depths between 1.1 m and 1.5 m, and formed the main failure surface for the LHS section.

All of these kinematic processes generated a differential acceleration of the slope surface as recorded by the photogrammetric cameras [1]. This is confirmed from plots of the sediment velocities on the LHS and RHS sections at the early stage of failure, i.e., at $t = 1.2$ s. This time $t = 1.2$ s was chosen to conincide with the time simulation F2 took to first mobilize the full failure surface.It is clear from Figure 17 that the sediment on the RHS section accelerated more rapidly than on the LHS section, in agreement with observed field measurements.

6 Debris flow with variable cohesion

For Simulation F2, we used the same material parameters as in the previous simulation, but varied the cohesion of the sediment to incorporate the effect

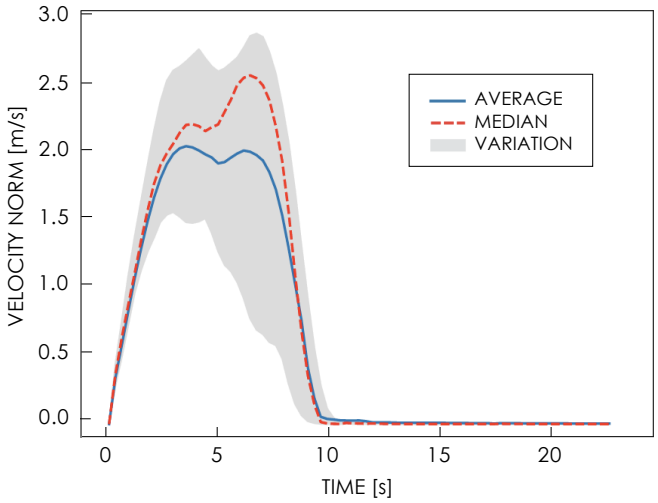

Fig. 16: Time series of the runout velocity for Simulation F1. The solid line is the average of the particles on the failure region, dashed line is the median, and the shaded area is the envelope of all velocities. Velocity norm = $\|\boldsymbol{v}\|$.

of variable root reinforcement. We emphasize that the objective of the simulation was not to capture the exact geometry of the failure scar, since that would take numerous iterations to back-figure the exact spatial distribution of cohesion that leads to the observed failure scar. Instead, the goal was simply to correlate the root reinforcement profile with the failure pattern observed at the Ruedlingen site. To this end, we refer once again to Figure 7, which shows the spatial distribution of cohesion adopted in the model. The central portion of the slope (dark blue area) had no root reinforcement, whereas a transition zone with a baseline cohesion of 700 Pa was included (light blue area). All the remaining parts of the slope had reinforcements of up to 90 kPa [51], but in our model a uniform value of 2 kPa was applied [3]. As before, the entire simulation ran for approximately $t = 20$ s of solution time.

6.1 Quantification of mobilized sediment

We begin by analyzing the projected failure area, mobilized volume, and the final sediment deposit calculated by the variable cohesion model. Figure 18 shows the horizontal projection of the simulated failure contour (labeled F2 scar) superimposed with the surveyed failure scar at Ruedlingen. For reference, this figure may be compared with Figure 7 for an assessment of the influence

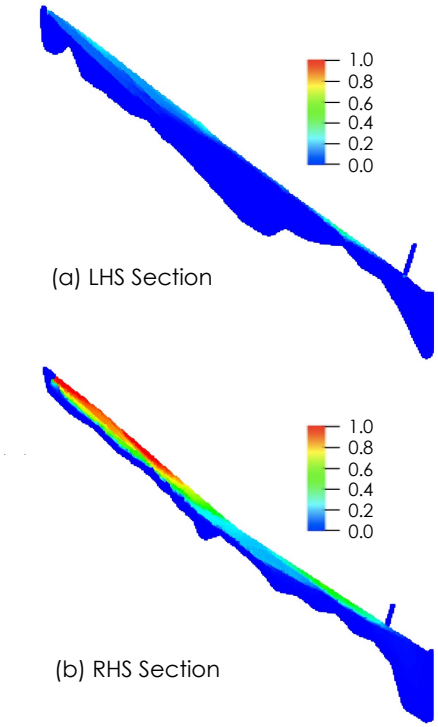

Fig. 17: Calculated sediment velocity $\|\boldsymbol{v}\|$ on longitudinal LHS and RHS sections of the slope at $t = 1.2$ s from Simulation F1. Color bar in m/s.

of cohesion on the geometry of the predicted failure scar. The total area of the F2 scar was approximately 174 m^2, which is 45% larger than the actual scar but 16% smaller than the F1 scar. Much like in the previous simulation, the sediment in the present simulation moved downwards in a slightly skewed fashion towards the RHS of the slope before coming to rest in front of the barrier.

Comparing the results of Simulations F1 and F2, it is now possible to see the influence of the heterogeneous root reinforcement on the shape of the failure scar. From Figure 18, it is evident that the mobilized contour covered a large portion of the area that had no root reinforcement. Failure of the slope started from the upper right portion as a result of the boundary conditions in that region. More importantly, from validation standpoint, the shape of the F2 scar is now much closer to the actual failure scar than was the shape of the F1 scar. In terms of total mobilized volume, approximately 160 m^3 was mobilized in Simulation F2, which is within 23% of error from the surveyed deposit at Ruedlingen.

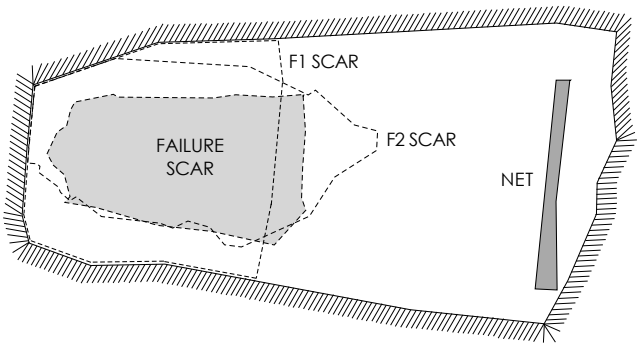

Fig. 18: Comparison of the actual failure scar and the scars predicted by Simulations F1 and F2.

Figures 19 and 20 show, respectively, the depositional configurations of the sediment on the longitudinal sections and transversal cross sections at the last time step. From the outset, we observe that the region corresponding to the failure surface surveyed at Ruedlingen (dark line) did not clear itself of sediment, but on the contrary, it was filled with sediment almost to the top. This is due to the effect of added cohesion in the sediment. As the failure advanced, the upper zones with higher cohesion moved over the depressions or cavities left by the sediment with lower cohesion. With the higher cohesion, they decelerated due to a "stick-slip" mechanism with the bedrock and the resistance imposed by the sediment right in front of them. In the end, even though the entire area depicted in Figure 18 had mobilized, the upper sediment had backfilled the depressions left by the lower sediment. A more refined modeling that would have cleared these cavities of backfilled sediment would have involved some form of cohesion softening on the particle response [8], but this was not pursued in the present work.

This leads us to an alternative way of validating our solution without the need to introduce cohesion softening into the computational framework, and that is to compare the failure scar at Ruedlingen directly with the zone of localized deformation within the slope [12]. Figures 21 and 22 depict the accumulated plastic strain on the longitudinal sections and transversal cross sections, respectively, at time $t = 1.2$ s (elapsed time until the whole failure surface was first mobilize for Simulation F2). As can be seen from these figures, the failure surfaces agree very well in terms of shape and depth, reaching the bedrock top as observed in the field. Another improvement due to the additional root reinforcement is visible on the debris that accumulated in front of the barrier. Taking a look at Figure 20d, we can see that the amount and shape of the deposit agree very well, with almost no excess sediment reaching the bottom of the slope.

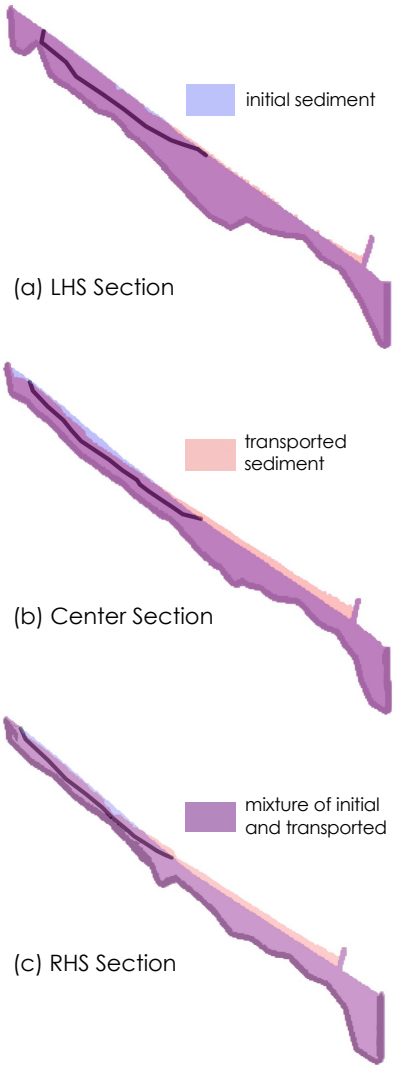

Fig. 19: Final configuration of sediment deposit on three longitudinal sections from Simulation F2. Black outline represents the failure surface surveyed at the Ruedlingen site.

6.2 Kinematics of the triggering and runout

Figure 23 shows the time evolution of the runout velocity for Simulation F2. Observe that both the average peak and maximum velocities are very similar to those obtained from Simulation F1, with values of approximately 2 m/s and

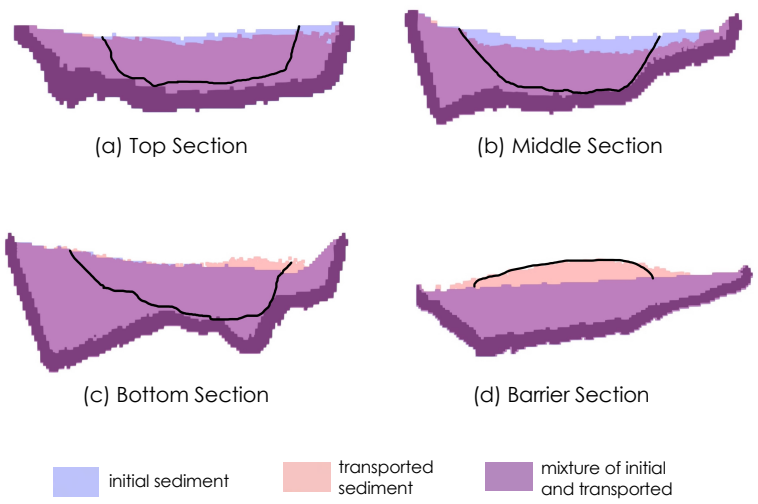

Fig. 20: Final configuration of sediment deposit on four transversal sections from Simulation F2. Black outlines represent the failure surface surveyed at the Ruedlingen site.

3 m/s, respectively. It is interesting to note that the "stick-slip" mechanism described in the previous section is also reflected in the distribution of velocities. In Figure 16 we can see that the velocity reached its peak mean value of around 2 m/s very quickly after initiation, and remained almost constant over a fairly significant period before slowing down. For Simulation F2, on the other hand, the distribution of velocity over time had two staggered stages. In the first stage, the velocity reached a peak mean value of around 1.5 m/s and remained constant for a while; then the flow accelerated once again, reaching a second peak of approximately 2 m/s. The flow also slowed down at a later time compared to Simulation F1, and had a more pronounced end tail, see Figure 23. In terms of flow duration, the total duration for Simulation F2, was approximately $t = 15$ s. This is 4 s longer than the time measured from the photogrammetric cameras, or a 36% difference. This difference is justified given that the real duration of the flow in the field is estimated using the photogrammetric cameras. However, this is an "external," visual perspective of failure. Our analysis on the other hand takes into consideration the kinematics of all particles to determine the simulated flow duration. Hence, there is some uncertainty associated with the real duration of the flow and no one-to-one correspondence between real and simulated flow durations.

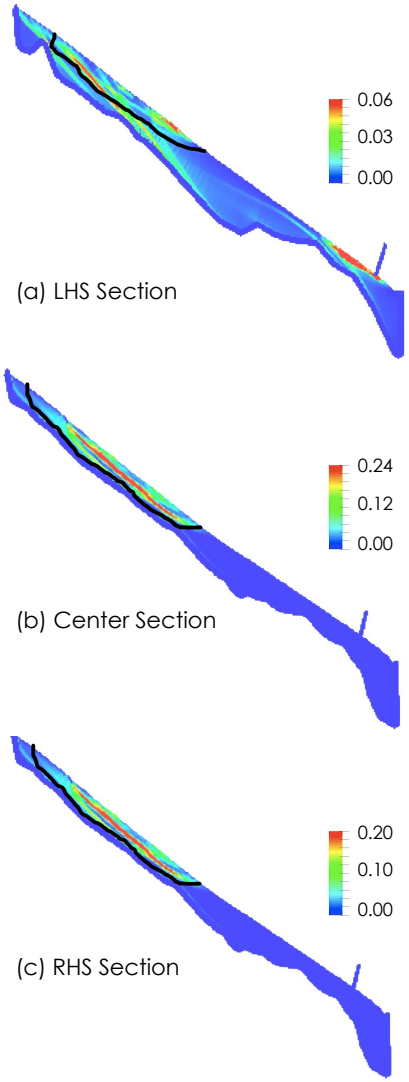

Fig. 21: Accumulated plastic strain at $t = 1.2$ s from Simulation F2. Black outline represents the failure surface surveyed at the Ruedlingen site. Color bar is norm of deviatoric plastic strain.

As a final point, we note that Simulation F2 also recovered the observed failure mechanism at the test slope, except that failure in the form of localized deformation initiated closer to the central portion rather than on the upper RHS of the slope. Failure for Simulation F2 now starts at about 96 cm below the surface, which is in very good agreement with the depth measured by in-

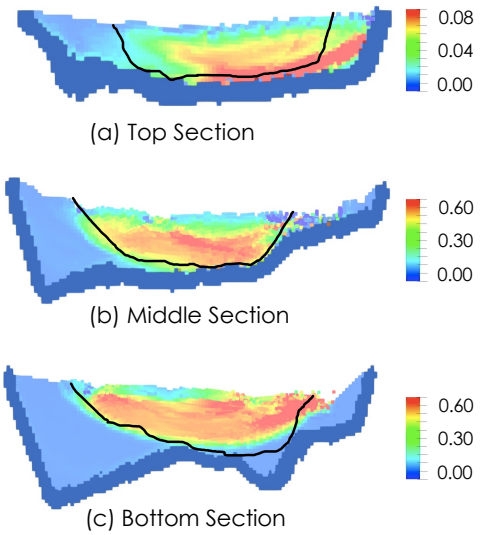

Fig. 22: Accumulated plastic strain at $t = 1.2$ s from Simulation F2. Black outline represents the failure surface surveyed at the Ruedlingen site. Color bar is norm of deviatoric plastic strain.

strumentation at Ruedlingen, of 80 cm. Figures 21 and 22 show that both the center and RHS sections have localized zones propagating all the way to the surface very early into the flow. However, the highest accumulation of plastic strain was near the bedrock interface for the top section and around 1.3 m below the surface for all transversal sections. This depth is consistent with the slope deformation data recorded at the test site [3]. Furthermore, consistent with the photogrammetric measurements, the flow accelerated differentially, with flow on the RHS accelerating faster than on the LHS. This is demonstrated in Figure 24, which presents the sediment velocities on the LHS and RHS longitudinal sections at $t = 1.2$ s.

A summary of the main results for Simulations F1 and F2 is shown in Table 3 alongside field measurements from Ruedlingen for easy comparison.

7 Summary and conclusions

Quantitative validation of debris flow models against field-scale data is very rare. Most work reported in the literature focused mainly on dry granular flows at the laboratory scale. The Ruedlingen test slope offers invaluable datasets against which any debris flow model may be validated quantitatively. The test

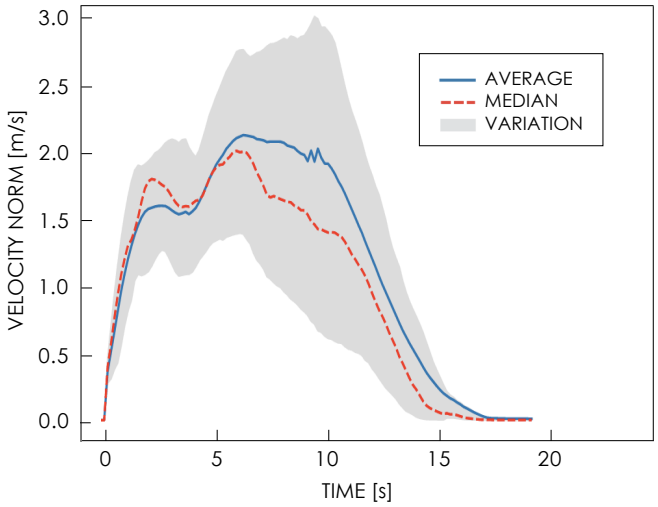

Fig. 23: Time series of the runout velocity for Simulation F2. The solid line is the average of the particles in the failure region, dashed line is the median, and the shaded area is the envelope of all velocities. Velocity norm = $\|\boldsymbol{v}\|$.

Table 3: Summary of the main results for Simulations F1 and F2.

Data	Ruedlingen	Simulation F1	Simulation F2
Area mobilized, m^2	120.0	200.9	174.3
Volume mobilized, m^3	130.0	190.0	160.0
Average flow velocity, m/s	1.5	1.6	1.1
Maximum flow velocity, m/s	3.0	2.9	3.0
Time to full mobilization, s	-	0.6	1.2
Duration, s	11.0	10.6	15.0
Initiation zone	Upper RHS	Upper RHS	Upper Center
Depth of initial shear zone, m	0.80	1.25	0.96
Shear band initiation time, s	-	0.3	0.6
Average shear band depth, m	1.30	1.28	1.12
Clear failure scar	Yes	Partially	No

slope not only covered very irregular topography, but the sediment was also extremely heterogeneous. Failure was triggered by a combination of natural and artificial causes, making the simulations more challenging. But the extensive instrumentation at the site made a detailed analysis of the debris flow processes for this field-scale test slope feasible.

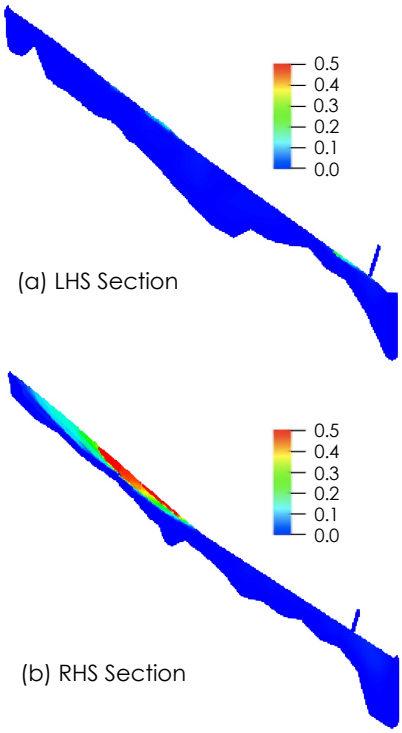

Fig. 24: Calculated sediment velocities on longitudinal LHS and RHS sections of the slope at $t = 1.2$ s from Simulation F2. Color bar in m/s.

Utilizing an updated Lagrangian scheme within the framework of SPH, we have conducted detailed 3D simulations of the debris flow processes for the Ruedlingen test slope. We have investigated, among other factors, the impacts of root reinforcement and complex bedrock and slope topography on the kinematics of progressive failure and runout.

In addition to results presented in Table 3, we have also investigated the runout path and final depositional configuration of the sediment at Ruedlingen. The discrepancies noted between predicted and observed final configurations of sediment deposit may be attributed to evolving sediment properties that have not been captured accurately in the simulations. For example, sediment having an initial cohesion due to partial saturation and root reinforcement may lose this cohesion when it becomes saturated and/or when the roots severed. Nevertheless, it is possible to predict the 3D geometry of the failure scar, even without the introduction of cohesion softening, by looking into the geometry of the zone of strain localization. Indeed, the proposed SPH

framework predicted zones of strain localization that agree quite well with the geometry of the observed failure scar at Ruedlingen.

Despite the encouraging results presented in this work, some aspects of the SPH solution can still be improved. Among them is the simulation of coupled solid deformation-fluid flow processes that could also take place within the sediment undergoing debris flow. Nevertheless, the work presented in this paper is significant in that it offered a unique opportunity to demonstrate how a debris flow model such as ours can be validated quantitatively against slope data at the field scale. Work is currently in progress to incorporate the aforementioned coupled processes within the Lagrangian framework of SPH.

Acknowledgements

This project was supported in part by the National Science Foundation under Award Number CMMI-1462231. The first author acknowledges the financial support of the National Council for Scientific and Technological Development of Brazil and the John A. Blume Earthquake Engineering Center. The experimental part of the research was partially funded by the Competence Centre for Environment and Sustainability (CCES) within the framework of the TRAMM – Project. Additional resources were provided by the ETH Research Fund and EU project SafeLand (EU FP7 grant agreement no. 226479).

References

[1] Askarinejad A, Akca D, Springman SM (2018) Precursors of instability in a natural slope due to rainfall: a full-scale experiment. Landslides, doi:10.1007/s10346-018-0994-0.

[2] Askarinejad, A, Springman, SM (2017) A novel technique to monitor subsurface movements of landslides. Canadian Geotechnical Journal, 55(5):620–630

[3] Askarinejad A (2013) Failure mechanisms in unsaturated silty sand slopes triggered by rainfall. Dr. Sc. Thesis No. 21423, ETH Zürich

[4] Askarinejad A, Casini F, Bischof P, Beck A, Springman SM (2012) Rainfall induced instabilities: a field experiment on a silty sand slope in northern Switzerland. Rivista Italiana di Geotecnica 3:50–71

[5] Bandara S, Ferrari A, Laloui L (2016) Modelling landslides in unsaturated slopes subjected to rainfall infiltration using material point method. Int J Num Analyt Meths Geomech 40(9):1358–1380

[6] Bonet J, Lok TSL (1999) Variational and momentum preservation aspects of smooth particle hydrodynamic formulations. Comput Methods Appl Mech Eng 180:97–115

[7] Borja RI, Choo J (2016). Cam-Clay plasticity. Part VIII: A constitutive framework for porous materials with evolving internal structure. Computer Methods in Applied Mechanics and Engineering 309:653–679
[8] Borja RI (2013). Plasticity Modeling and Computation, Springer-Verlag, Berlin-Heidelberg
[9] Borja RI, Song X, Wu W (2013) Critical state plasticity. Part VII: Triggering a shear band in variably saturated porous media. Computer Methods in Applied Mechanics and Engineering 261–262:66–82
[10] Borja RI, Liu X, White J, (2012) Multiphysics hillslope processes triggering landslides. Acta Geotechnica 7(4):261–269
[11] Borja RI, White J, Liu X, Wu W (2012) Factor of safety in a partially saturated slope inferred from hydro-mechanical continuum modeling. International Journal for Numerical and Analytical Methods in Geomechanics 36(2):236–248
[12] Borja RI, White J (2010) Continuum deformation and stability analyses of a steep hillside slope under rainfall infiltration. Acta Geotechnica 5(1):1–14
[13] Borja RI, Andrade JE (2006) Critical state plasticity. Part VI: Meso-scale finite element simulation of strain localization in discrete granular materials. Computer Methods in Applied Mechanics and Engineering 195:5115–5140
[14] Borja RI (2004) Cam-Clay plasticity. Part V: A mathematical framework for three-phase deformation and strain localization analyses of partially saturated porous media. Computer Methods in Applied Mechanics and Engineering 193:5301–5338
[15] Borja RI, Tamagnini C (1998) Cam-Clay plasticity, Part III: Extension of the infinitesimal model to include finite strains. Computer Methods in Applied Mechanics and Engineering 155:73–95
[16] Bui HH, Fukugawa R (2013) An improved SPH method for saturated soils and its application to investigate the mechanisms of embankment failure: Case of hydrostatic pore-water pressure. International Journal for Numerical and Analytical Methods in Geomechanics 37:31–50
[17] Bui HH, Fukugawa R, Sako K, Wells C (2011) Slope stability analysis and discontinuous slope failure simulation by elasto-plastic smoothed particle hydrodynamics (SPH). Géotechnique 361(7):565–574
[18] Bui HH, Fukugawa R, Sako K, Ohno S (2008) Lagrangian meshfree particles method (SPH) for large deformation and failure flows of geomaterial using elastic-plastic soil constitutive model. International Journal for Numerical and Analytical Methods in Geomechanics 32:1537–1570
[19] Bui HH, Sako K, Fukugawa R (2007) Numerical simulation of soil-water interaction using smoothed particle hydrodynamics (SPH) method. Journal of Terramechanics 44:339–346
[20] Calvetti F, di Prisco C, Redaelli I, Sganzerla A, Vairaktaris E (2019) Mechanical interpretation of dry granular masses impacting on rigid obstacles. Acta Geotechnica https://doi.org/10.1007/s11440-019-00831-9

[21] Casini F, Jommi C, Springman S (2010) A laboratory investigation on an undisturbed silty sand from a slope prone to landsliding. Granular Matter 12(3):303–316

[22] Chen W, Qiu T (2011) Numerical Simulations of Granular Materials using Smoothed Particle Hydrodynamics Method. Geotechnical Special Publication ASCE 217:157–164

[23] Chen JS, Pan C, Wu CT, Liu WK (1996) Reproducing kernel particle methods for large deformation analysis of non-linear structures. Comput Methods Appl Mech Eng 139(1–4):195–227

[24] Desrues J, Argilaga A, Caillerie D, Combe G, Nguyen TK, Richefeu V, Pont SD (2019) From discrete to continuum modelling of boundary value problems in geomechanics: An integrated FEM-DEM approach. International Journal for Numerical and Analytical Methods in Geomechanics 43:919–955

[25] Fávero Neto AH (2019). A new computational framework for modeling granular fiows. PhD Thesis, Stanford University, California, USA.

[26] Fávero Neto AH, Borja RI (2018) Continuum hydrodynamics of dry granular flows employing multiplicative elastoplasticity. Acta Geotechnica 13(5):1027–1040

[27] Fern EJ, Soga K (2015) The role of constitutive models in MPM simulations of granular column collapses. Acta Geotech 11(3):659–678

[28] He X, Liang D (2015) Study of the runout of granular columns with SPH methods. Int J Offshore Polar Engrg 25(4):281–287

[29] He X, Liang D, Wu W, Cai G, Zhao C, Wang S (2018) Study of the interaction dry granular flows and rigid barriers with an SPH model. International Journal for Numerical and Analytical Methods in Geomechanics 42(11):1217–1234

[30] Iverson R (1997) The physics of debris flows. Reviews of Geophysics 35(3):245–296

[31] Kermani E, Qiu T (2019) Simulation of quasi-static axisymmetric collapse of granular columns using smoothed particle hydrodynamics and discrete element methods. Acta Geotechnica, https://doi.org/10.1007/s11440-018-0707-9

[32] Korzani MG, Galindo-Torres SA, Scheuermann A, Williams DJ (2018) SPH approach for simulating hydro-mechanical processes with large deformations and variable permeabilities. Acta Geotechnica 13:303–316

[33] Kuhn MR, Prunier F, Daouadji A (2019) Stiffness pathologies in discrete granular systems: Bifurcation, neutral equilibrium, and instability in the presence of kinematic constraints. International Journal for Numerical and Analytical Methods in Geomechanics 43:888–918

[34] Lai X, Ren B, Fan H, Li S, Wu CT, Regueiro RA, Liu L (2015) Peridynamics simulations of geomaterial fragmentation by impulse loads. Int J Num Analyt Meths Geomech 39(12):1304–1330

[35] Lee J, Hong J-W (2019) Morphological aspects of crack growth in rock materials with various flaws. International Journal for Numerical and Analytical Methods in Geomechanics 43:1854–1866

[36] Lehmann, P, Gambazzi, F, Suski, B, Baron, L, Askarinejad, A, Springman, SM, Holliger, K & Or, D (2013). Evolution of wetting patterns preceding hydro-mechanically induced landslide inferred from electrical resistivity tomography. Water Resources Research, 49(12):7992–8004

[37] Liang W, Zhao J (2019). Multiscale modeling of large deformation in geomechanics. International Journal for Numerical and Analytical Methods in Geomechanics 43:1080–1114

[38] Longo A, Pastor M, Sanavia L, Manzanal D, Stickle MM, Lin C, Yague A, Tayyebi SM (2019) A depth average SPH model including $\mu(I)$ rheology and crushing for rock avalanches. International Journal for Numerical and Analytical Methods in Geomechanics 43:833-857

[39] Liu GR, Liu, MB (2003) Smoothed particle hydrodynamics: a meshfree particle methods. World Scientific, Singapore

[40] Lucy LB (1977) A numerical approach to the testing of the fission hypothesis. The Astronomical Journal 82(12):1013–1024

[41] Monaghan J (1992) Smoothed particle hydrodynamics. Annual Review of Astronomy and Astrophysics 30(1):543–574

[42] Monaghan J, Gingold R (1983) Shock simulation by the particle method SPH. Journal of Computational Physics 52(2):374–389

[43] Mondal S, Olsen-Kettle L, Gross L (2019) Simulating damage evolution and fracture propagation in sandstone containing preexisting 3-D surface flaw under uniaxial compression. International Journal for Numerical and Analytical Methods in Geomechanics 43(7):1448-1466

[44] Moriguchi S, Borja RI, Yashima A, Kazuhide S (2009) Estimating the impact force generated by granular flow on a rigid obstruction. Acta Geotechnica 4:57–71

[45] Nonoyama H, Moriguchi S, Sawada K, Yashima A (2015) Slope stability analysis using smoothed particle hydrodynamics (SPH) method. Soils and Foundations 55(2):458–470

[46] Pastor M, Yague A, Stickle MM, Manzanal D, Mira P (2018) A two-phase SPH model for debris flow propagation. International Journal for Numerical and Analytical Methods in Geomechanics 42(3):418–448

[47] Peng C, Wang S, Wu W, Yu H-S, Wang C, Chen J-Y (2019) LOQUAT: an open-source GPU-accelerated SPH solver for geotechnical modeling. Acta Geotechnica https://doi.org/10.1007/s11440-019-00839-1

[48] Peng C, Guo X, Wu W, Wang Y (2016) Unified modelling of granular media with Smoothed Particle Hydrodynamics. Acta Geotechnica 11:1231–1247

[49] Peng C, Wu W, Yu HS, Wang C (2015) A SPH approach for large deformation analysis with hypoplastic constitutive model. Acta Geotechnica 10:703–717

[50] Rabczuk T, Belytschko T, Xiao SP (2004) Stable particle methods based on Lagrangian kernels. Computer Methods in Applied Mechanics and Engineering, 193(12-14):1035–1063

[51] Schwarz M (2011) Hydro-mechanical characterization of rooted hill slope failure: from field investigations to fiber bundle modeling. Dr. Sc. Thesis No. 19124, ETH Zürich, Switzerland

[52] Semnani SJ, White JA, Borja, RI (2016) Thermo-plasticity and strain localization in transversely isotropic materials based on anisotropic critical state plasticity. International Journal for Numerical and Analytical Methods in Geomechanics 40:2423–2449

[53] Shiozawa S, Lee S, Wheeler MF (2019) The effect of stress boundary conditions on fluid-driven fracture propagation in porous media using a phase-field modeling approach. International Journal for Numerical and Analytical Methods in Geomechanics 43:1316–1340

[54] Sibille L, Villard P, Darve F, Hosn RA (2019) Quantitative prediction of discrete element models on complex loading paths. International Journal for Numerical and Analytical Methods in Geomechanics 43:858–887

[55] Simo JC, Hughes TJR (1998). Computational Inelasticity, Springer-Verlag, Berlin-Heidelberg

[56] Siriaksorn T, Chi S-W, Foster C, Mahdavi A (2018) *u-p* semi-Lagrangian reproducing kernel formulation for landslide modeling. Int J Num Analyt Meths Geomech 42(2):231–255

[57] Sitarenios, P, Casini, F, Askarinejad, A, Springman, SM (2019) Hydro-mechanical analysis of a surficial landslide triggered by rainfall: the Ruedlingen case history. Géotechnique

[58] Song X, Menon S (2019) Modeling of chemo-hydromechanical behavior of unsaturated porous media: a nonlocal approach based on integral equations. Acta Geotechica 14:727–747

[59] Song X, Khalili N (2019) A peridynamics model for strain localization analysis of geomaterials. International Journal for Numerical and Analytical Methods in Geomechanics 43:77–96

[60] Song X, Wang K, Ye M (2018) Localized failure in unsaturated soils under non-isothermal conditions. Acta Geotechnica 13:73–85

[61] Song X, Borja RI (2014) Mathematical framework for unsaturated flow in the finite deformation range. International Journal for Numerical Methods in Engineering 14:658–682

[62] Sparks PA, Sherburn JA, Heard WF, Williams BA (2019). Penetration modeling of ultra-high performance concrete using multiscale meshfree methods. International Journal for Numerical and Analytical Methods in Geomechanics 43(14):2328–2351

[63] Springman, SM, Askarinejad, A, Casini, F, Friedel, S, Kienzler, P, Teysseire, P, Thielen, A (2012) Lessons learnt from field investigations in potentially unstable slopes in Switzerland. Slovenian Geotechnical Journal 9(1):5–29

[64] Sulsky, D, Chen, Z, Schreyer, HL (1994) A particle method for history-dependent materials. Comput Methods Appl Mech Eng 118(1–2):179–196
[65] Świtała BM, Askarinejad, A, Wu, W, Springman, SM (2018). Experimental validation of a coupled hydro-mechanical model for vegetated soil. Géotechnique 68(5):375–385, doi:10.1680/jgeot.16
[66] Takahashi T (2014) Debris flow: mechanics, prediction and countermeasures, 2nd Edition. CRC Press, UK
[67] Teufelsbauer H, Wang Y, Pudasaini SP, Borja RI, Wu W (2011) DEM simulation of impact force exerted by granular flow on rigid structures. Acta Geotechnica 6:119–133
[68] Turco E, dell'Isola F, Misra A (2019) A nonlinear Lagrangian particle model for grains assemblies including grain relative rotations. International Journal for Numerical and Analytical Methods in Geomechanics 43:1051–1079
[69] Vidal Y, Bonet J, Huerta A (2007) Stabilized updated Lagrangian corrected SPH for explicit dynamic problems. Int J Numer Methods Eng 69:2687–2710
[70] Vignjevic R, Reveles JR, Campbell J (2006) SPH in a total Lagrangian formalism. Comput Model Eng Sci 14(3):181–198
[71] Violeau D (2012) Fluid mechanics and the SPH method: theory and applications. Oxford University Press, UK
[72] Yan B, Regueiro RA (2019) Three-dimensional discrete element method parallel computation of Cauchy stress distribution over granular materials. International Journal for Numerical and Analytical Methods in Geomechanics 43:974–1004
[73] Zhang Q, Choo J, Borja RI (2019). On the preferential flow patterns induced by transverse isotropy and non-Darcy flow in double porosity media. Computer Methods in Applied Mechanics and Engineering 353:570–592
[74] Zhao S, Bui HH, Lemiale V, Nguyen GD, Darve F (2019) A generic approach to modelling flexible confined boundary conditions in SPH and its application. International Journal for Numerical and Analytical Methods in Geomechanics 43:1005–1031
[75] Zhao Y, Semnani SJ, Yin Q, Borja RI (2018) On the strength of transversely isotropic rocks. International Journal for Numerical and Analytical Methods in Geomechanics 42:1917–1934